Nuclear matter equation of state from a quark-model nucleon-nucleon interaction

K. Fukukawa,[1,2,*] M. Baldo,[1] G. F. Burgio,[1] L. Lo Monaco,[3] and H.-J. Schulze[1]
[1]*INFN Sezione di Catania, Via Santa Sofia 64, I-95123 Catania, Italy*
[2]*Research Center for Nuclear Physics, Osaka University, 10-1 Mihogaoka, Osaka 567-0047, Japan*
[3]*Dipartimento di Fisica, Università di Catania, Via Santa Sofia 64, I-95123 Catania, Italy*
(Received 28 July 2015; revised manuscript received 12 October 2015; published 17 December 2015)

Starting from a realistic constituent quark model for the nucleon-nucleon interaction, we derive the equation of state (EOS) of nuclear matter within the Bethe-Brueckner-Goldstone approach up to the three-hole-line level, without the need to introduce three-nucleon forces. To estimate the uncertainty of the calculations both the gap and the continuous choices for the single-particle potential are considered and compared. The resultant EOS is compatible with the phenomenological analysis of the saturation point, the incompressibility, the symmetry energy at a low density, and its slope at saturation, together with the high-density pressure extracted from flow data on heavy-ion collisions. Although the symmetry energy is appreciably higher in the gap choice in the high-density region, the maximum neutron star masses derived from the continuous-choice EOS and the gap-choice EOS are similar and close to two solar masses, which is again compatible with recent observational data. A comparison with other microscopic equations of state is presented and discussed.

DOI: 10.1103/PhysRevC.92.065802 PACS number(s): 13.75.Cs, 21.65.Mn, 26.60.Kp

I. INTRODUCTION

The nuclear matter equation of state (EOS) is one of the central issues in nuclear physics. Detailed knowledge of it would allow us to connect the data obtained in laboratory experiments on heavy-ion collisions (HICs) and the processes that characterize the structure and evolution of compact astrophysical objects like neutron stars (NSs) and supernovas. On the other hand, laboratory experiments and astrophysical observations can put meaningful constraints on the nuclear EOS. Unfortunately, a direct link between phenomenology and the EOS is not possible and theoretical frameworks and inputs are necessary for the interpretation of the data. In particular, the EOS above saturation density is much less constrained than that around or below saturation.

For several years, intense activity has been focused on analyzing and interpreting the experimental and observational data for the purpose of putting severe constraints on the EOS and on the corresponding theoretical models [1]. It can be recognized from these efforts that a sound theoretical and microscopical framework for modeling the EOS can be of help for the establishment of firm results on EOS properties. Along these lines a microscopic many-body theory based on interactions among nucleons, which stems from strong interaction theory, can be of great relevance in reducing the uncertainties that characterize this type of analysis.

Meson-exchange models of the nucleon interaction have been extensively developed for several years and applied to nuclear matter and NS structure within many-body theory. Among them are the variational method [2], the relativistic Dirac-Brueckner-Hartree-Fock (DBHF) [3], and the nonrelativistic Bethe-Brueckner-Goldstone (BBG) expansion [4–7], which have employed different versions of nucleon-nucleon interactions inspired by the meson-exchange model. In the nonrelativistic scheme three-body forces (TBFs) have been introduced to obtain the correct saturation point of nuclear matter [8–11]. The goal of all these approaches is to devise an elementary interaction among nucleons that is able to describe both few-body nuclear systems and nuclear matter in agreement with the existing phenomenological data. This program has been only partially successful. It turns out, in fact, that it is difficult to reproduce the binding energy of three- and four-body systems and, at the same time, to predict the correct saturation point within this scheme.

More recently the chiral expansion theory on nucleon interaction has been extensively developed [12–24]. This approach is based on a deeper level of the strong-interaction theory, where QCD chiral symmetry is explicitly exploited in a low-momentum expansion of multinucleon interaction processes. In this approach multinucleon interactions arise naturally and a hierarchy of the different orders can be established. Despite some ambiguity in the parametrization of the force [23] and some difficulty in the treatment of many-body systems [25], the method has enabled great progress in the microscopic theory of nuclear systems. Indeed it turns out [24,26] that within this class of interactions a compatible treatment of few-nucleon systems and nuclear matter is possible. Along the same lines, a chiral force [27] has been adjusted to reproduce, within a Monte Carlo calculation, the binding of ^{4}He and the phase shifts of neutron-α scattering. The same interaction was used to describe neutron matter. Coupled cluster calculations with chiral forces including TBFs have been performed for neutron and symmetric nuclear matter [28,29], and finite nuclei [30].

Another approach inspired by the QCD theory of strong interaction has been developed by a few groups [31–37]. In this approach the quark degree of freedom is explicitly introduced and the nucleon-nucleon interaction is constructed from gluon and meson exchange between quarks, the latter being confined inside the nucleons. One of these quark models of the nucleon-nucleon interaction, called fss2 [37,38], is able to reproduce closely the experimental phase shifts and few-body binding

*fukukawa@rcnp.osaka-u.ac.jp

energies [38–41]. More recently it has been shown [42] that the fss2 interaction is able to reproduce also the correct nuclear matter saturation point without any additional parameter or need to introduce TBFs.

In this paper we analyze further the fss2 interaction. On one hand, we compare the results in nuclear matter with additional phenomenological constraints; on the other hand, we extend the EOS based on the fss2 interaction to a higher density and apply it to NS calculations. In this study we use the renormalized energy-independent kernel of this model [43]. Kernels of quark-model nucleon-nucleon interactions are obtained by using the resonating-group method (RGM) for the $(3q)$-$(3q)$ system. Although they are therefore energy dependent, we can eliminate the energy dependence, as we see in the next section.

This paper is organized as follows. In Sec. II we introduce the quark-model nucleon-nucleon interaction fss2 [38,44] and the formulation for the renormalized RGM kernel. We briefly review phase shifts and deuteron properties. The explicit form of the deuteron wave function is given in the Appendix. In Sec. III we first recapitulate the Brueckner-Hartree-Fock (BHF) calculation and the Bethe-Faddeev calculation, based on the BBG framework [45]. Then the nuclear matter EOS for the fss2 interaction is reported and its properties are discussed in relation to the phenomenological constraints, also in comparison with some other theoretical methods and interactions. Section IV is devoted to calculations of the NS structure. Conclusions are drawn in Sec. V.

II. QUARK-MODEL BARYON-BARYON INTERACTION FSS2

The fss2 baryon-baryon interaction [38,44] is a low-energy effective model, which introduces some essential features of QCD. The color degree of freedom is explicitly considered within the spin-flavor SU(6) approximation and the antisymmetrization of quarks is exactly taken into account within the framework of the RGM. The full model Hamiltonian for the $(3q)$-$(3q)$ system reads

$$H = \sum_{i=1}^{6}\left(m_i + \frac{p_i^2}{2m_i}\right) - T_G + \sum_{i<j}^{6}\left(U_{ij}^{\mathrm{Cf}} + U_{ij}^{\mathrm{FB}} + U_{ij}^{\mathrm{S}} + U_{ij}^{\mathrm{PS}} + U_{ij}^{\mathrm{V}}\right), \quad (1)$$

where m_i and p_i are the constituent quark mass and momentum of each particle, respectively, and T_G denotes the center-of-mass motion. The remaining terms denote the effective quark-quark interaction.

The confinement potential U_{ij}^{Cf} is a phenomenological r^2-type potential, which has the favorable feature that it does not contribute to baryon-baryon interactions. We use a color analog of the Fermi-Breit (FB) interaction U_{ij}^{FB} with explicit quark-mass dependence, motivated by the dominant one-gluon exchange process in conjunction with the asymptotic freedom of QCD. This includes the short-range repulsion and spin-orbit force, both of which are successfully described. On the other hand, the medium-range attraction and the long-range tensor force, especially those mediated by pions, are extremely nonperturbative from the viewpoint of QCD. These are therefore most relevantly described by effective meson-exchange potentials. Compared with the previous-version FSS [46,47], in which scalar (S) and pseudoscalar (PS) nonets are included, the introduction of vector (V) nonets and the momentum-dependent Bryan-Scott term [48] greatly improves nucleon-nucleon phase shifts [38] and makes fss2 sufficiently realistic. The RGM equation for the relative wave function $\chi(\boldsymbol{r})$ is given by

$$\langle\phi(3q)\phi(3q)|E - H|\mathscr{A}\{\phi(3q)\phi(3q)\chi(\boldsymbol{r})\}\rangle = 0, \quad (2)$$

where $\phi(3q)$ is the three-quark cluster (nucleon) wave function and is described by a $(0s)^3$ harmonic oscillator with a common width parameter. The antisymmetrization operator is denoted $\mathscr{A}$. In our actual calculation, Eq. (2) is solved in momentum space [49]. We rewrite Eq. (2) in Schrödinger-like form as

$$[\varepsilon - H_0 - V_{\mathrm{RGM}}(\varepsilon)]\chi(\boldsymbol{r}) = 0, \quad (3)$$

where ε is the two-nucleon energy measured from its threshold in the center-of-mass system and H_0 is the kinetic energy operator. We regard $V_{\mathrm{RGM}}(\varepsilon) = V_D + G + \varepsilon K$ as the nonlocal and energy-dependent potential. Here, V_D is the direct meson-exchange kernel, G represents all exchange kernels for the kinetic energy and interaction terms, and K is the exchange normalization kernel.

In the many-body scattering problem, an energy-independent potential is desirable, since the energy of a two-nucleon pair is not well defined in the in-medium scattering state. The energy dependence of the RGM kernel can be reduced by renormalizing the RGM kernel in the following way [50]. We can rewrite Eq. (3) as

$$[\varepsilon - N^{-1/2}(H_0 + V_D + G)N^{-1/2}]\Psi(\boldsymbol{r}) = 0, \quad (4)$$

where

$$N \equiv \langle\phi(3q)\phi(3q)|\mathscr{A}|\phi(3q)\phi(3q)\rangle \quad (5)$$

is the normalization kernel and $\Psi(\boldsymbol{r}) \equiv N^{1/2}\chi(\boldsymbol{r})$ is the renormalized RGM wave function. If we define the nonlocal kernel

$$W \equiv N^{-1/2}(H_0 + V_D + G)N^{-1/2} - (H_0 + V_D + G) \quad (6)$$

and the renormalized RGM potential $V^{\mathrm{RGM}} \equiv V_D + G + W$, then Eq. (3) becomes

$$[\varepsilon - H_0 - V^{\mathrm{RGM}}]\Psi(\boldsymbol{r}) = 0. \quad (7)$$

The detailed procedure to calculate W can be found in Appendix A in Ref. [43]. The asymptotic behavior of $\Psi(\boldsymbol{r})$ is the same as that of $\chi(\boldsymbol{r})$, because the square root of the normalization kernel approaches unity at large distances. The phase shifts derived from $\Psi(\boldsymbol{r})$ are the same as those from $\chi(\boldsymbol{r})$.

In this study, we use a Gaussian representation of the fss2 potential for numerical simplicity [51]. This representation conserves the nonlocal feature of the potential accurately and reproduces the original phase shifts within an accuracy better than 0.1° for almost all energies and partial waves. The

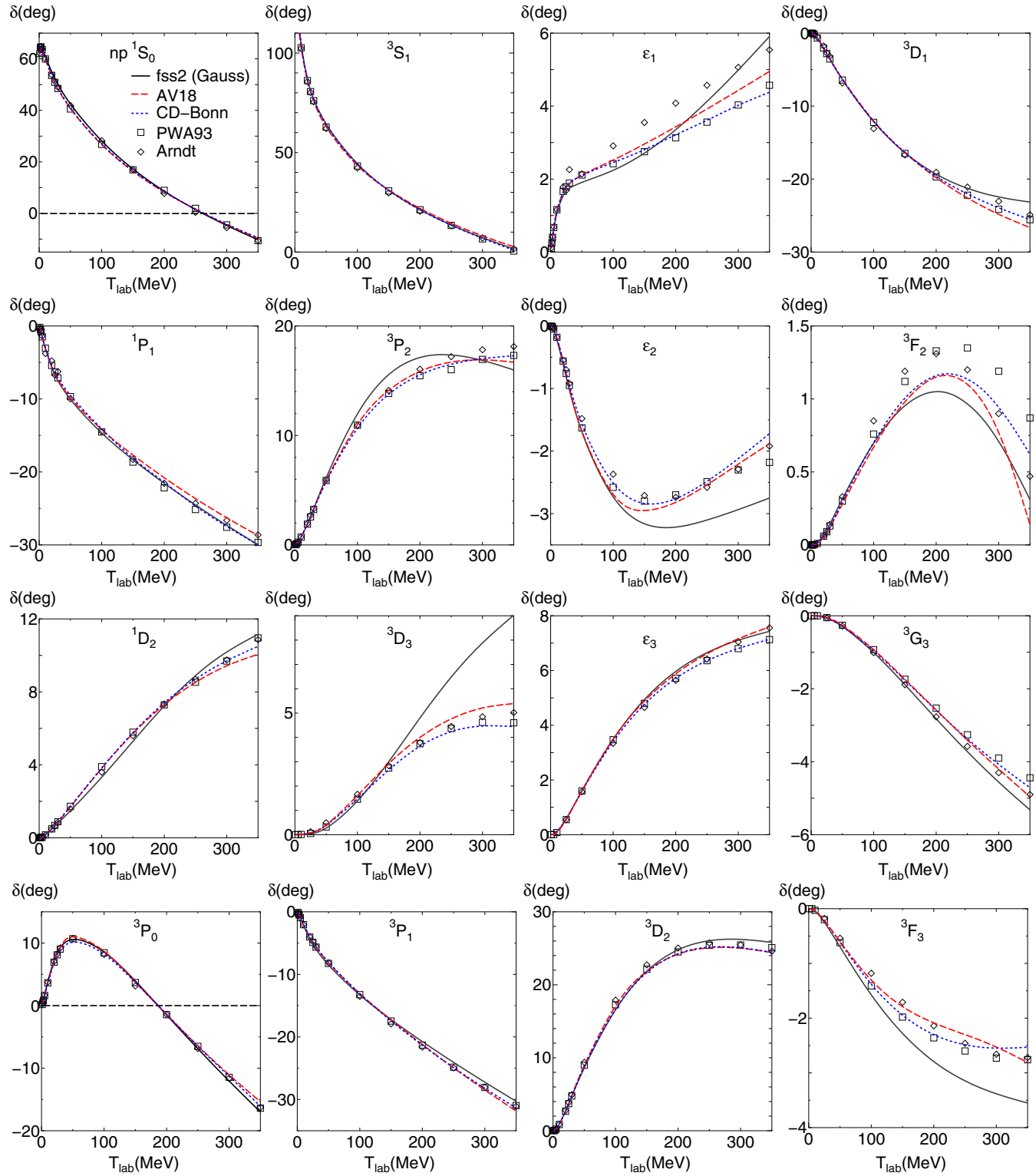

FIG. 1. (Color online) Phase shifts of the energy-independent Gaussian fss2 potential up to the energy $T_{lab} \leqslant 350$ MeV (solid black curves) compared with the results for the Argonne V18 [52] [long-dashed (red) curves)] and CD-Bonn [53] [short-dashed (blue) curves] potentials. Symbols show results from the Nijmegen multienergy phase shift analysis [54,55] and Arndt's *np* phase shift analyses [56–59].

energy dependence of the Gaussian-represented potential is eliminated by the above-mentioned method. The phase shifts for the energy-independent version of fss2 are shown in Fig. 1. One can note some deficiencies in the $^3P_2$ and $^3F_{2,3}$ phase shifts. As pointed out in Ref. [38], this is probably related to the problem of the balance of central and LS force in the short-range region. Appreciable deviations appear also in the $^3D_1$ and $^3D_3$ channels in the higher-energy region. This implies

TABLE I. Neutron-proton phase shifts and proton-proton $^1S_0$ phase shifts (in deg) and χ^2 values of the fss2 model with respect to the Nijmegen phase shift analysis.

	$T_{\rm lab}$ (MeV)									
	0.383	1	5	10	25	50	100	150	215	320
No. of data	144	68	103	290	352	572	399	676	756	954
$\Delta\chi^2$	3034	2100	274	710	919	6804	1409	3913	1464	2637
$^1S_0(pp)$	14.519	33.097	55.765	56.601	50.693	41.324	27.350	16.822	6.143	−7.090
$^1S_0(np)$	54.592	62.220	64.223	60.862	52.234	41.916	27.496	16.899	6.130	−7.105
$^3S_1$	159.429	147.838	118.380	102.881	80.956	63.014	43.191	30.495	18.540	4.737
ε_1	0.027	0.103	0.653	1.116	1.678	1.915	2.209	2.684	3.553	5.344
$^3P_0$	0.048	0.195	1.747	3.885	8.546	11.250	9.038	4.018	−3.147	−14.100
$^3P_1$	−0.030	−0.122	−1.033	−2.249	−5.228	−8.685	−13.448	−17.273	−21.786	−28.502
$^1P_1$	−0.049	−0.193	−1.545	−3.183	−6.703	−10.267	−14.826	−18.392	−22.502	−28.421
$^3P_2$	0.005	0.020	0.237	0.682	2.573	6.252	12.412	15.901	17.485	16.592
ε_2	0.000	−0.002	−0.057	−0.207	−0.824	−1.767	−2.854	−3.218	−3.211	−2.865
$^3D_1$	−0.001	−0.005	−0.183	−0.679	−2.821	−6.519	−12.427	−16.596	−20.160	−22.872
$^3D_2$	0.001	0.006	0.221	0.842	3.671	8.825	17.091	22.260	22.562	26.213
$^1D_2$	0.000	0.001	0.045	0.162	0.635	1.473	3.294	5.304	7.816	10.677
$^3D_3$	0.000	0.000	0.001	0.001	0.008	0.192	1.287	2.975	5.361	8.425
ε_3	0.000	0.000	0.013	0.081	0.554	1.625	3.570	5.008	6.250	7.271
$^3F_2$	0.000	0.000	0.002	0.013	0.101	0.319	0.718	0.978	1.076	0.595
$^3F_3$	0.000	0.000	−0.005	−0.033	−0.230	−0.703	−1.612	−2.315	−2.940	−3.471
$^1F_3$	0.000	0.000	−0.011	−0.066	−0.424	−1.156	−2.344	−3.194	−4.028	−5.094
$^3F_4$	0.000	0.000	0.000	0.001	0.017	0.087	0.366	0.816	1.642	3.455
ε_4	0.000	0.000	0.000	−0.004	−0.047	−0.191	−0.540	−0.866	−1.223	−1.642
$^3G_3$	0.000	0.000	0.000	−0.004	−0.054	−0.264	−0.982	−1.882	−3.109	−4.889
$^3G_4$	0.000	0.000	0.001	0.014	0.171	0.726	2.191	3.673	5.423	7.716
$^1G_4$	0.000	0.000	0.000	0.003	0.038	0.147	0.386	0.606	0.886	1.413
$^3G_5$	0.000	0.000	0.000	0.000	−0.009	−0.052	−0.189	−0.316	−0.399	−0.279
ε_5	0.000	0.000	0.000	0.002	0.037	0.206	0.733	1.300	1.983	2.917

that improvements of the tensor force are desirable in future refinements of the interaction.

Examining χ^2 with respect to the phase shift analysis is a good test to see how strictly the interaction describes the observables. In this study, we worked in the isospin basis and with the cutoff Coulomb force,

$$V_C(k) = \frac{1-\cos(kR_{\rm cut})}{k^2}, \tag{8}$$

and extracted the nuclear phase shifts using the Vincent-Phatak method [60]. This method gives stable phase shifts with respect to the change in $R_{\rm cut}$ [61], which we take as $R_{\rm cut} = 10$ fm.

Another important factor in considering the pp phase shifts is charge-independence breaking. The charge-independence-breaking effect is taken into account by a reduction factor for the coupling constant of the scalar-singlet meson, which is determined to minimize χ^2 [38,41]. Our value of the reduction factor is 0.9932, which is quite close to the 0.9934 used in Ref. [41]. We report in Table I the neutron-proton (np) and the $^1S_0$ proton-proton (pp) phase shifts, along with their $\Delta\chi^2$ values with respect to the Nijmegen phase shift analysis [55,62]. The Gaussian fss2 potential gives $\chi^2/N_{\rm data} = 6.34$. Although the phase shifts are overall well reproduced, as we saw in Fig. 1, we have larger χ^2 values, mainly due to the $^3P_2$, $^1D_2$, and $^3D_3$ partial waves in the high-energy region. Moreover, the constraint for the $^1S_0$ pp phase shifts in the low-energy region is very severe. Those phase shifts given by the Nijmegen phase shift analysis are 14.609° and 32.688° at $E_p = 0.383$ and 1 MeV, respectively [62]. A more developed treatment is desirable, because the difference from the Nijmegen phase shift analysis should be much less than 0.1°.

When the deuteron properties were determined in Appendix B in Ref. [38], the authors first solved Eq. (3) for $\chi(\boldsymbol{r})$ and then obtained the renormalized relative wave function $\Psi(\boldsymbol{r}) = N^{1/2}\chi(\boldsymbol{r})$. For the renormalized potential, we can directly solve Eq. (4) for $\Psi(\boldsymbol{r})$. Because the procedure to obtain the potential and that to obtain the deuteron wave function are different, it is necessary to reexamine the deuteron properties. The detailed prescription is explained in the Appendix.

Figures 2 and 3 show the deuteron wave functions by the energy-independent fss2 potential in coordinate and momentum space, respectively. The wave functions are indistinguishable from those in Ref. [38]. It can also be seen in Table II that the renormalization of the kernel does not change the deuteron properties. Our calculation slightly underpredicts the quadrupole moment, as other potentials do. According to Refs. [63] and [64], the correction due to the meson-exchange current is typically about 0.01 fm^2. However, even taking this correction into account, there is still a small discrepancy.

TABLE II. Comparison of the deuteron properties with the predictions using fss2, Bonn C, CD-Bonn, and experimental (expt.) data.

	fss2-Gauss	fss2 (isospin) [38]	Bonn C [65]	CD-Bonn [53]	Expt.
ε_d (MeV)	2.2206	2.2250	Fitted	Fitted	2.224644 ± 0.000046 [66]
$R_{\rm rms}$ (fm)	1.961	1.960	1.968	1.966	1.971 ± 0.006 [67–69]
Q_d (fm^2)	0.270	0.270	0.281	0.270	0.2859 ± 0.0003 [70,71]
$\eta = A_D/A_S$	0.0252	0.0253	0.0266	0.0256	0.0256 ± 0.0004 [72]
P_D (%)	5.52	5.49	5.60	4.85	

III. NUCLEAR MATTER EOS WITHIN THE BETHE-BRUECKNER-GOLDSTONE APPROACH

A. Sketch of the approach

The basis of the BHF calculation is the Bethe-Goldstone equation for the G matrix,

$$\langle 12|G(\omega)|34\rangle_A = \langle 12|V|34\rangle_A + \sum_{5,6}\langle 12|V|56\rangle \frac{Q_{56}}{\omega - e_5 - e_6}\langle 56|G(\omega)|34\rangle_A, \tag{9}$$

where the multi-indices 1,2, . . . include the momentum and the spin-isospin variables of the particles, $|12\rangle_A \equiv |12\rangle - |21\rangle$, V is the bare nucleon-nucleon interaction, ω is the starting energy, and $Q_{56} \equiv \Theta(k_5 - k_F^{(5)})\Theta(k_6 - k_F^{(6)})$ is the two-particle Pauli operator, where $k_F^{(i)}$ are the Fermi momenta of the nucleons. In this study, we use the angle-averaged form of the Pauli operator and the two-particle intermediate energy $e_5 + e_6$, in order to avoid the complex coupling of the angular-momentum quantum numbers [73].

The single-particle (s.p.) energy is defined by $e_i = k_i^2/2M_N + U_i(k_i)$, where M_N is the nucleon mass. The auxiliary s.p. potentials $U_i(k_i)$ are self-consistently determined by the on-shell G matrix elements, with Eq. (9):

$$U_i(k_i) = \sum_{j<k_F}\langle ij|G(e_i + e_j)|ij\rangle_A. \tag{10}$$

The s.p. potential $U(k)$ can be chosen in various ways. Our investigations are carried out for two somewhat opposite choices: the continuous choice and the gap (or standard) choice. In the continuous choice, Eq. (10) is solved for all k, while $U(k) = 0$ is assumed for $k > k_F$ in the gap choice. The detailed procedure for BHF calculations is presented in Refs. [45] and [74].

In this study, we calculate the binding energy per particle for symmetric nuclear matter (SNM) $E/A(\rho, x_p = 0.5)$ and pure neutron matter (PNM) $E/A(\rho, x_p = 0)$, where $x_p = \rho_p/\rho$ is the proton fraction. In these cases the energy per particle from the two-hole-line contribution is given by

$$\left(\frac{E}{A}\right)_2 = \frac{3}{5}\frac{k_F^2}{2M_N} + \frac{1}{2\rho}\sum_{k<k_F} U(k). \tag{11}$$

At a given baryonic density ρ, we approximate E/A for asymmetric nuclear matter by the parabolic approximation,

$$\frac{E}{A}(\rho, x_p) = (1-\beta)\frac{E}{A}\Big|_{\rm SNM}(\rho) + \beta\frac{E}{A}\Big|_{\rm PNM}(\rho), \tag{12}$$

where $\beta = (1 - 2x_p)^2$, which has been verified to be a good approximation within the BHF approach [75].

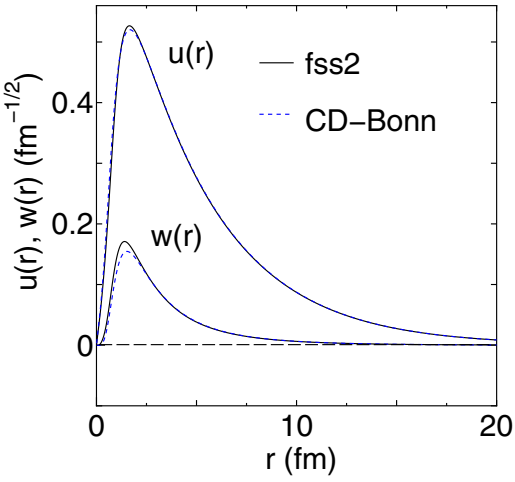

FIG. 2. (Color online) Deuteron wave functions $u(r) = u_{0\alpha}(r)$ and $w(r) = u_{2\alpha}(r)$ predicted by the energy-independent Gaussian potential based on fss2 (solid black curve) compared with CD-Bonn [dashed (blue) curve] [53].

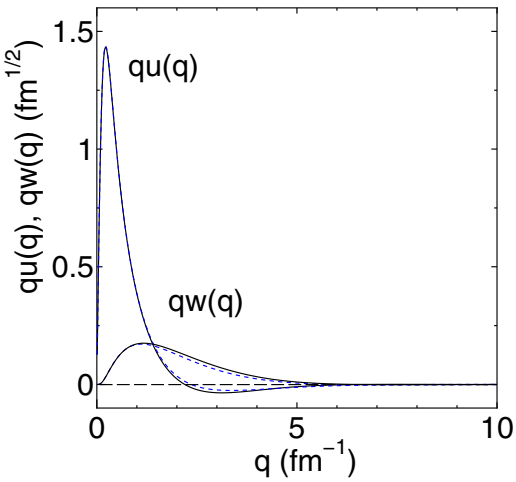

FIG. 3. (Color online) Same as Fig. 2, but for deuteron wave functions in momentum space $qu(q) = qf_{0\alpha}(q)$ and $qw(q) = qf_{2\alpha}(q)$.

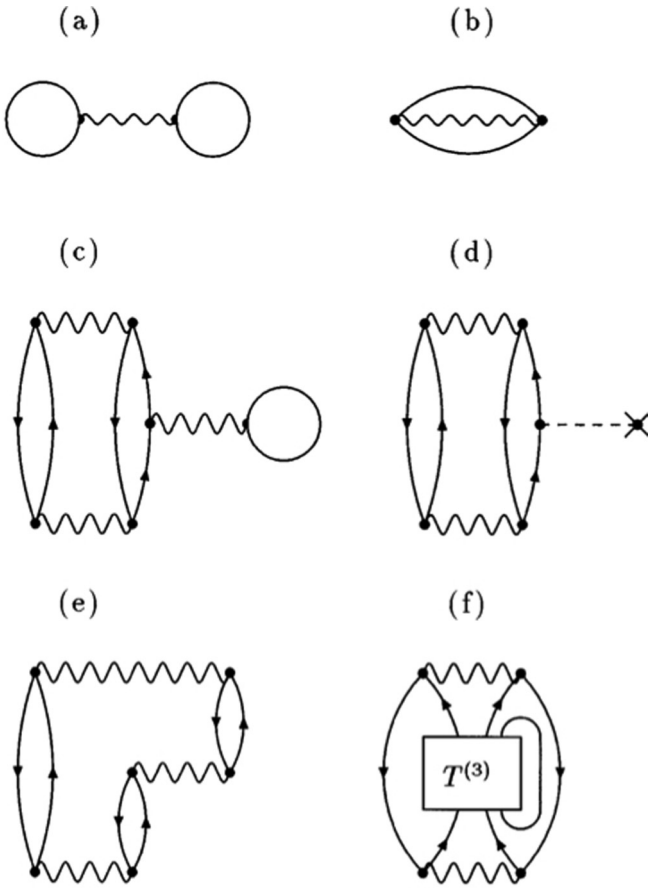

FIG. 4. Goldstone diagrams contributing to the nuclear matter EOS. Diagrams (a) and (b) correspond to the BHF calculation. The sum of the other diagrams gives the three-hole-line contribution. For details, please see the text.

The two-hole-line and three-hole-line (THL) diagrams are depicted in Fig. 4, where the wavy line denotes the G matrix. Figures 4(a) and 4(b) are the above-mentioned BHF direct (Hartree) and exchange (Fock) diagrams, respectively. As for the THL calculations, we closely follow the method described in detail in Ref. [4]. The full scattering process of three particles that are virtually excited above the Fermi sphere can be calculated by solving the Bethe-Faddeev equation for the in-medium three-body scattering matrix $T^{(3)}$, as depicted in Fig. 4(f) [4,45,76]. For computational convenience, the lowest-order contribution in the G matrix, namely, Fig. 4(c), is calculated separately. Figure 4(c) is known as the "bubble" diagram, and Fig. 4(d) is the corresponding U-insertion diagram. Note that the U-insertion diagram vanishes in the gap choice, because $U(k) = 0$ is assumed for $k > k_F$. Figure 4(e) is the "ring" diagram, which is responsible for long-range correlations in nuclear matter. An indication of convergence of the BBG expansion is the possible small size of the THL contribution with respect to the two-hole-line contribution.

B. Numerical results

We report in Tables III–VI the contributions of each diagram to the equations of state (EOSs) for SNM and PNM with the continuous and gap choice, respectively. The slightly different results with respect to Ref. [42] are due to the more refined momentum grid we used in the present calculations. This was relevant at a higher density in order to obtain convergence in the BHF iteration procedure. We divide the space of relative momentum q into two domains, $[0,a]$ and $[a,\infty]$, and apply the Gauss-Legendre quadrature to each part in solving the Bethe-Goldstone equation. The mapping $q = a + \tan[(1+x)\pi/4]$, where x are the nodes of the Gauss-Legendre quadrature, is used for the second part as in Ref. [49]. In this study, $a = 6$ fm^{-1} is adopted and we take 70 points in the first section and 30 points in the second section. All nucleon-nucleon channels up to the total angular momentum $J = 8$ were considered. In each iteration, the s.p. potential was calculated self-consistently up to $k_{\max} = 7.5$ fm^{-1}, with a grid step of 0.1 fm^{-1}. After 30 iterations, a convergence within a few keV was reached in all calculations at $k_F \leqslant 3.0$ fm^{-1}.

After adding the THL contributions, we fitted the calculated EOSs, for both SNM and PNM, by an analytic form with four parameters:

$$\frac{E}{A}(\rho) = a\rho + b\rho^c + d. \tag{13}$$

The values of the fitted parameters are listed in Table VII. These fitted EOSs are valid for densities that are not too low, $\rho \gtrsim 0.1$ fm^{-3}, and must not be extrapolated to zero density. The fitted EOSs, for both nuclear matter and PNM, are used for NS calculations. In this case the low-density region will be described by the crust EOS, where the fitted nuclear matter EOS is not used. With the continuous choice around saturation the analytic form is very close to the calculated points, and one can extract the saturation energy $(E/A)_0 = -16.3$ MeV at $\rho_0 = 0.157$ fm^{-3} and an incompressibility $K = 219$ MeV, while with the gap choice one finds $(E/A)_0 = -15.6$ MeV, $\rho_0 = 0.170$ fm^{-3}, and $K = 185$ MeV. This indicates the uncertainty of the EOS around saturation. At a higher density the fit is less precise, but the deviation does not exceed 1.2 MeV even at the highest density with the continuous choice, which is more than enough for NS calculations. With the gap choice, it is not as easy to describe the EOS by one single analytic expression from very low to high densities as with the continuous choice, but the reported values of the parameters give a good fit at high densities, which is useful for the NS study.

The fss2 EOSs for SNM and PNM are reported in Fig. 5, in comparison with the corresponding EOSs from some other approaches. The latter have been selected from those that are able to reproduce the saturation point within the phenomenological uncertainty. The comparison of the different EOSs for SNM shows a substantial agreement up to about 0.5 fm^{-3}, while at higher densities both the variational calculation (APR) in Ref. [2] and the relativistic DBHF calculation in Ref. [3] indicate a stiffer trend. As for nonrelativistic BHF calculations, also the EOS obtained with a "microscopic" TBF in Refs. [10] and [11] is appreciably stiffer in that density region, while the BHF with the Urbana model [8,9] for the TBF produces an EOS in substantial agreement with the fss2 EOS. A similar trend is present in PNM.

TABLE III. Energies per nucleon (in MeV) of the various THL contributions to the SNM EOS for different Fermi momenta k_F (in fm^{-1}). The continuous choice is adopted. The baryon density $\rho = 2k_F^3/(3\pi^2)$ (in fm^{-3}) is also listed. $T + E_2$ corresponds to the BHF calculations; B, the bubble diagram; BU, the U-insertion diagram; R, the ring diagram; H, higher-order diagrams; E_3, the total THL contribution.

k_F	ρ	$T + E_2$	B	BU	R	$H \times 10^3$	E_3	$T + E_2 + E_3$
1.1	0.090	−17.07	−7.14	11.02	−0.77	186.8	3.30	−13.77
1.2	0.117	−19.58	−6.17	11.46	−1.27	159.3	4.22	−15.36
1.3	0.148	−21.98	−4.37	11.68	−1.63	113.8	5.79	−16.19
1.4	0.185	−24.21	−2.33	12.48	−1.87	77.22	8.35	−15.86
1.5	0.228	−26.91	0.80	12.93	−1.99	48.35	11.79	−14.30
1.6	0.277	−27.41	4.93	13.91	−2.13	26.58	16.73	−10.67
1.7	0.332	−27.90	10.76	14.83	−2.05	10.88	23.56	−4.34
1.8	0.394	−27.33	18.91	15.61	−1.93	1.19	32.59	5.27
1.9	0.463	−25.57	29.85	16.21	−1.75	−3.75	44.31	18.74
2.0	0.540	−22.25	43.71	15.09	−1.42	2.49	57.39	35.14
2.1	0.626	−17.08	61.42	13.52	−1.29	0.80	73.66	56.57
2.2	0.719	−9.73	83.58	10.47	−1.19	−0.11	92.86	83.13
2.3	0.822	−0.01	111.12	6.15	−1.11	−0.21	116.16	116.16

TABLE IV. Same as Table III, but with the gap choice for the s.p. potential.

k_F	ρ	$T + E_2$	B	R	$H \times 10^3$	E_3	$T + E_2 + E_3$
1.1	0.090	−11.54	−0.48	−1.00	65.07	−1.42	−12.95
1.2	0.117	−13.45	0.08	−1.09	49.27	−0.96	−14.41
1.3	0.148	−15.26	1.02	−1.18	33.16	−0.13	−15.39
1.4	0.185	−16.86	2.48	−1.22	20.72	1.28	−15.59
1.5	0.228	−18.12	4.64	−1.25	11.66	3.40	−14.72
1.6	0.277	−18.88	7.82	−1.29	5.45	6.54	−12.34
1.7	0.332	−19.00	12.40	−1.26	0.99	11.14	−7.85
1.8	0.394	−18.31	18.96	−1.24	−1.99	17.72	−0.59
1.9	0.463	−16.65	28.03	−1.19	−3.96	26.84	10.19
2.0	0.540	−13.90	39.71	−1.09	−1.80	38.62	24.73
2.1	0.626	−9.90	55.18	−1.06	−1.83	54.12	44.22
2.2	0.719	−4.53	75.75	−1.95	−1.76	74.71	70.17
2.3	0.822	2.29	102.63	−1.06	−1.56	101.57	103.85

TABLE V. Same as Table III, but for PNM.

k_F	ρ	$T + E_2$	B	BU	R	$H \times 10^3$	E_3	$T + E_2 + E_3$
1.0	0.034	5.18	−0.84	1.17	−0.01	2.63	0.33	5.50
1.1	0.045	5.96	−0.85	1.38	−0.11	−0.04	0.42	6.38
1.2	0.058	6.83	−0.76	1.53	−0.15	−3.74	0.62	7.45
1.3	0.074	7.66	−0.63	1.84	−0.15	−7.02	1.04	8.71
1.4	0.093	8.55	−0.38	2.14	−0.15	−9.34	1.60	10.15
1.5	0.114	9.56	0.07	2.41	−0.13	−10.59	2.34	11.90
1.6	0.138	10.71	0.74	2.81	−0.10	−11.32	3.44	14.14
1.7	0.166	12.10	1.79	3.25	−0.09	−11.17	4.94	17.04
1.8	0.197	13.87	3.40	3.66	−0.09	−10.39	6.96	20.83
1.9	0.232	16.05	5.69	4.11	−0.09	−8.81	9.70	25.75
2.0	0.270	18.76	8.74	4.30	−0.05	−5.54	12.98	31.74
2.1	0.313	22.23	12.81	4.39	−0.07	−4.17	17.13	39.36
2.2	0.360	26.61	18.92	4.14	−0.08	−2.99	22.97	49.59
2.3	0.411	32.02	24.66	3.66	−0.10	−2.09	28.22	60.23
2.4	0.467	38.53	33.09	2.76	−0.10	−1.33	35.74	74.28
2.5	0.528	46.42	43.30	1.18	−0.11	−0.75	44.36	90.79
2.6	0.594	55.86	55.46	−1.08	−0.13	−0.39	54.25	110.11
2.7	0.665	66.93	70.50	−4.14	−0.14	−0.15	66.22	133.15
2.8	0.741	79.78	89.54	−8.23	−0.15	−0.09	81.16	160.94
2.9	0.824	94.52	110.30	−13.50	−0.27	0.42	96.53	191.05

TABLE VI. Same as Table V, but with the gap choice for the s.p. potential.

k_F	ρ	$T+E_2$	B	R	$H\times10^3$	E_3	$T+E_2+E_3$
1.0	0.034	5.79	−0.23	−0.05	1.03	−0.28	5.51
1.1	0.045	6.70	−0.18	−0.08	−0.82	−0.26	6.43
1.2	0.058	7.63	−0.09	−0.10	−2.68	−0.18	6.51
1.3	0.074	8.62	0.07	−0.09	−4.21	−0.03	8.59
1.4	0.093	9.69	0.32	−0.09	−5.10	0.23	9.91
1.5	0.114	10.88	0.71	−0.07	−5.42	0.63	11.50
1.6	0.138	12.25	1.30	−0.06	−5.56	1.24	13.49
1.7	0.166	13.88	2.19	−0.05	−5.45	2.14	16.02
1.8	0.197	15.85	3.53	−0.05	−5.16	3.47	19.32
1.9	0.232	18.24	5.43	−0.06	−4.60	5.37	23.61
2.0	0.270	21.15	7.95	−0.05	−3.11	7.90	29.06
2.1	0.313	24.69	11.34	−0.06	−2.41	11.28	35.97
2.2	0.360	28.96	15.89	−0.08	−1.79	15.19	44.77
2.3	0.411	34.40	21.76	−0.09	−1.26	21.67	55.71
2.4	0.467	40.02	29.50	−0.10	−0.83	29.40	69.43
2.5	0.528	47.00	39.64	−0.12	−0.47	39.53	86.52
2.6	0.594	55.02	52.63	−0.14	−0.24	52.49	107.51
2.7	0.665	64.13	69.74	−0.16	−0.06	69.58	133.71
2.8	0.741	74.37	93.04	−0.19	−0.05	92.85	167.22
2.9	0.824	85.70	123.18	−0.21	0.08	122.97	208.67

In Fig. 5 the EOS is reported in the density range relevant for NS calculations. From Tables III–VI one can note that at the highest densities the THL contribution can be larger than the two-hole-line one. This makes the convergence of the BBG expansion at least questionable. However, it turns out that the two-hole-line interaction part is quite limited because of the strong compensation between negative and positive channel contributions, and actually it is decreasing in the highest density region. On the contrary, the dominant contribution to the THL interaction term comes from the repulsive "bubble" diagram. This consideration suggests that the convergence might still be present, but of course it does not give a strong argument in support of it.

TABLE VII. Fitted coefficients in Eq. (13) for SNM and PNM and the continuous (C) or gap (G) choice, together with those obtained for other interactions.

	a	b	c	d
SNM				
C	−515.4	692.6	1.30	2.4
G	−113.6	296.4	1.91	−6.2
PNM				
C	−103.5	355.3	1.48	8.3
G	60.2	252.3	2.50	3.4
SNM				
APR	−101.5	333.9	2.14	−4.8
DBHF	−422.8	711.3	1.56	7.3
V18 + TBF	−123.2	407.9	2.38	0.0
V18 + UIX	−137.0	308.0	1.82	−5.0
PNM				
APR	76.1	256.5	2.71	3.6
DBHF	−230.3	715.5	1.58	9.5
V18 + TBF	55.9	532.3	2.68	0.0
V18 + UIX	11.0	309.0	1.95	6.0

However, in addition to that, one can see in Tables III–VI that three-body scattering processes, described by the scattering matrix $T^{(3)}$ (column "H"), give a negligible contribution. It can then be expected that four-body scattering processes will also be negligibly small. The fourth-order diagrams, apart from the four-body scattering processes, have been estimated in Ref. [77] up to about three times saturation density for the Reid soft-core NN interaction [78] and found to be quite small. We assume that this is also true in our case, even for higher densities, at least approximately enough for NS calculations.

As a check of this assumption we confront the EOS with known phenomenological constraints. The higher-density part of the EOS, needed for NS calculations, can be seen as an extrapolation from the lower one, which can be validated by a comparison with astrophysical observations and laboratory experiments on HICs. It is clear that the main theoretical uncertainty in the EOS indeed comes from the many-body calculations at higher densities. Unfortunately it is difficult to get a quantitative estimate of this uncertainty without a firm limit on the higher-order contributions beyond the THL.

C. Comparison with phenomenology

We now confront the EOS with a set of phenomenological constraints in order to assess its reliability. Possible tests of the EOS have been devised from experiments on HICs, which have been performed in the last two decades at energies ranging from a few tens to several hundred MeV per nucleon. It can be expected in fact that in HICs at a high enough energy nuclear matter is compressed and that the two partners of the collisions produce flows of matter. In principle, the dynamics of the collisions should be connected with the properties of the nuclear medium EOS and its viscosity. In the so-called

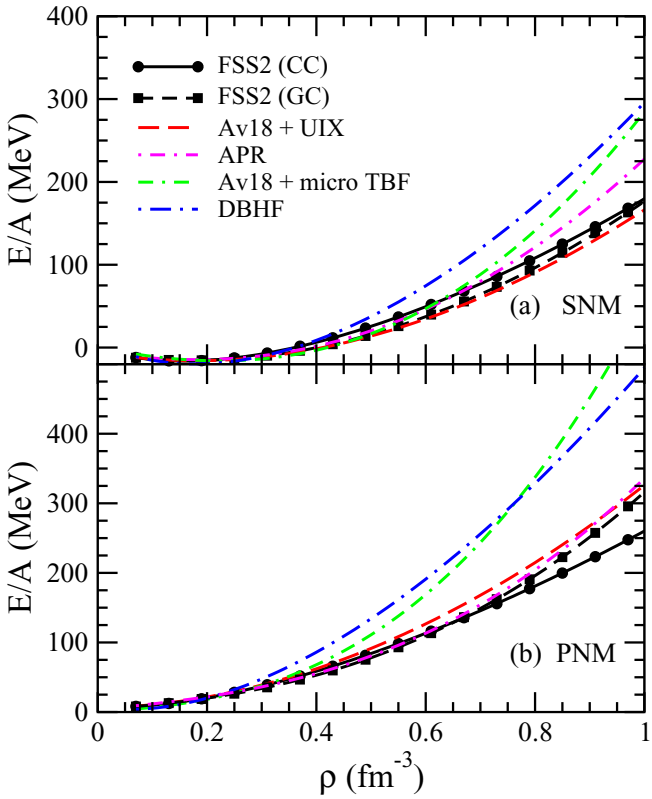

FIG. 5. (Color online) The energy per particle of SNM (top) and PNM (bottom) for several EOSs as a function of the baryon density. Curves FSS2 (CC) and FSS2 (GC) show the calculated fss2 EOS with the continuous and gap choice, respectively. Curve $Av_{18}+$UIX refers to the BHF calculation using Argonne V18 plus Urbana IX TBFs from Refs. [8] and [9], curve APR is the variational calculation from Ref. [2], curve $Av_{18}+$micro TBF is the BHF calculation from Refs. [10] and [11], and curve DBHF is the relativistic DBHF calculation from Ref. [3].

"multifragmentation" regime, after the collision numerous nucleons and fragments of different sizes are emitted, and the transverse flow, which is strongly affected by the matter compression during the collision, can be measured. Based on numerical simulations, it was proposed in Ref. [79] that any reasonable EOS for SNM should pass through a phenomenological region in the pressure vs density plane.

The plot is reproduced in Fig. 6, where a comparison with the same microscopic calculations is made. The larger shaded (yellow) band represents the results of numerical simulations of the experimental data discussed in Ref. [79], and the smaller shaded (violet) band represents the constraints from the experimental data on kaon production [80]. The fss2 EOS is in any case fully compatible with the phenomenological constraints. This is true also for the other selected EOSs, with the possible exception of the DBHF one, which appears too repulsive at higher densities. The analysis indicates that the EOS at low densities must be relatively soft.

Another gross property of the nuclear EOS, which plays a decisive role in NS calculations, is the symmetry energy as a function of the density $S(\rho)$, especially at the high density typical of the NS inner core. It can be expressed in terms of

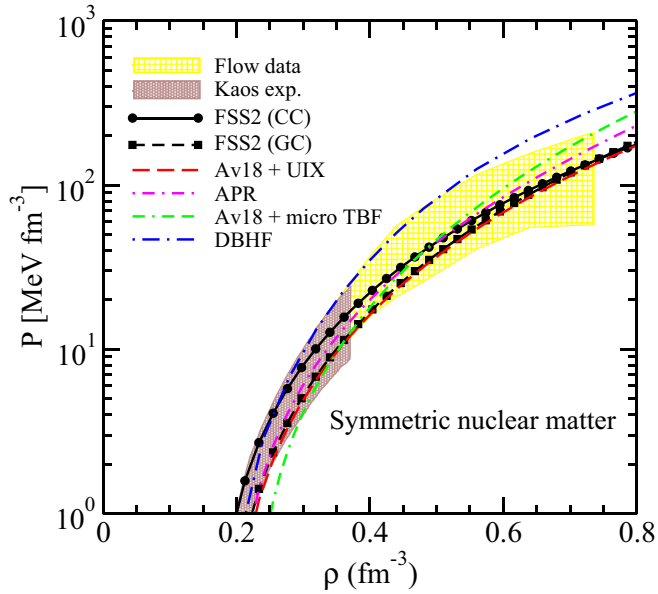

FIG. 6. (Color online) Pressure of symmetric matter for several EOSs. The larger shaded (yellow) and smaller shaded (violet) bands represent the phenomenological constraints from experimental data. See text for details.

the energy per particle between PNM and SNM,

$$S(\rho) = -\frac{1}{4}\frac{\partial(E/A)}{\partial x}(\rho,0.5) \approx \frac{E}{A}(\rho,0) - \frac{E}{A}(\rho,0.5), \quad (14)$$

and is reported in Fig. 7 for the considered set of EOSs. A large spread of values is present for densities above saturation. In comparison with the other EOSs, the fss2 EOS appears in the region of lower values ("isosoft" EOS), but the gap and continuous choices show an appreciable discrepancy at higher densities. As we will see, the stiffness of NS matter shows a reduced spread of values, since the β-equilibrium condition

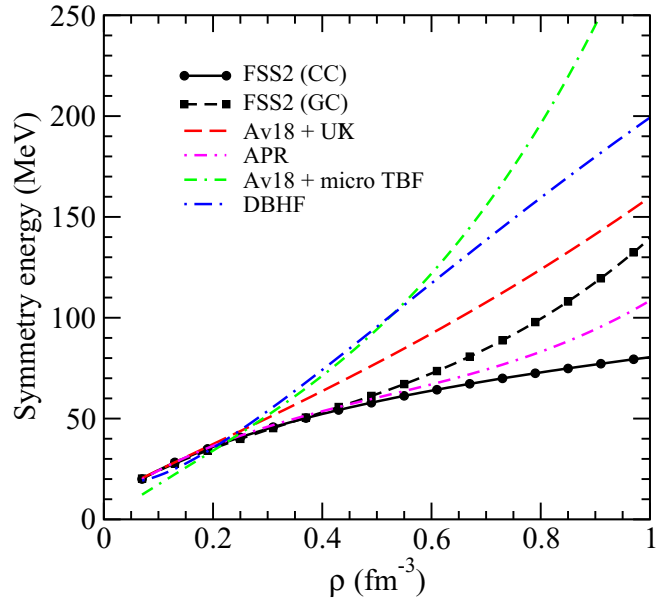

FIG. 7. (Color online) Symmetry energy for several EOSs.

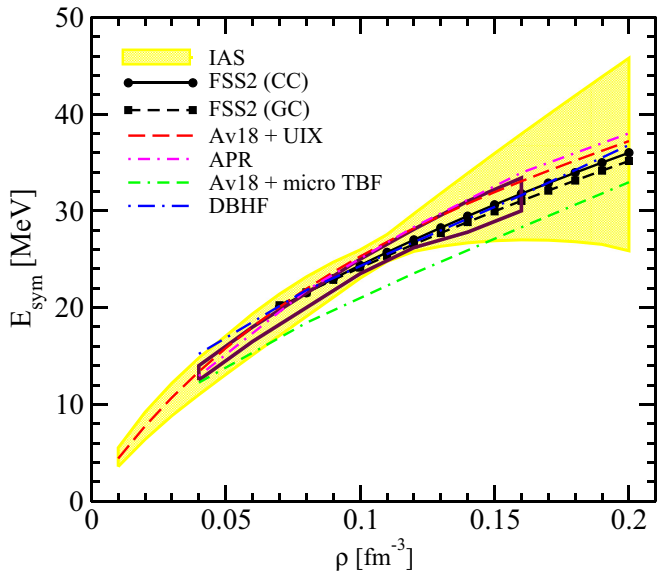

FIG. 8. (Color online) Symmetry energy at a low density. The shaded (yellow) band represents recent constraints [81] and the solid (brown) line shows the region restricted by the neutron skin data, whereas the different curves are the results of the microscopic many-body methods.

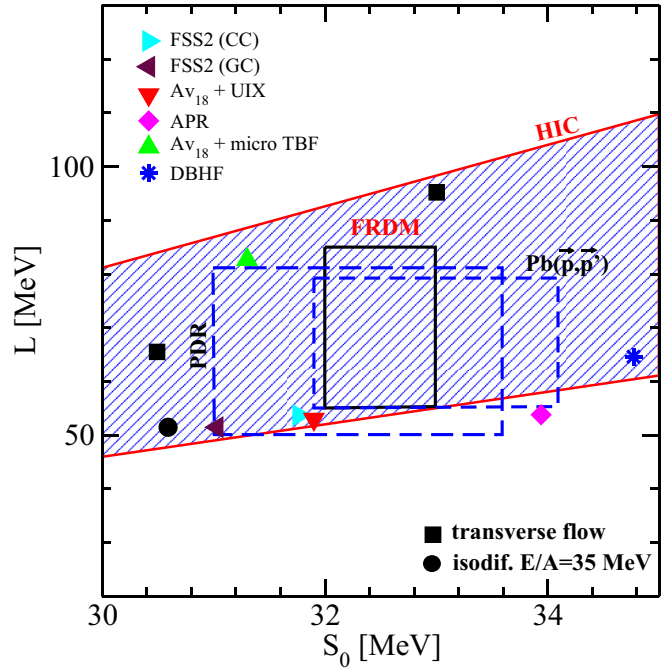

FIG. 9. (Color online) $L = 3\rho(\partial S/\partial\rho)|_{\rho=\rho_0}$ versus symmetry energy at saturation S_0, predicted by several EOSs. See text for details of the experimental constraints.

produces a compensation effect due to the interplay of the size of the symmetry energy and the stiffness of the EOS.

The symmetry energy up to saturation density has been constrained in Ref. [81] by analyzing the data on isobaric analog states as well as those on the neutron skin in a set of nuclei. In Fig. 8 the larger shaded (yellow) band indicates the constraint coming from the analog states, while the more restricted region bounded by the solid (brown) line is obtained if the neutron skin data are also added. The fss2 EOS is consistent throughout the constrained regions. The other EOSs also appear to be consistent with the constraints, with the possible exception of the BHF calculation with microscopic TBF.

Another parameter which characterizes the symmetry energy is its slope at saturation, usually embodied in the quantity $L \equiv 3\rho(\partial S/\partial\rho)|_{\rho=\rho_0}$. In Fig. 9 this parameter is displayed versus the value of the symmetry energy at saturation $S_0 \equiv S(\rho_0)$, which has been thoroughly discussed in Ref. [82]. The different boxes indicate several constraint regions obtained in different phenomenological analyses. The shaded (blue) band represents the constraint coming from experimental data on HICs, obtained from the neutron and proton spectra from central collisions for ^{124}Sn + ^{124}Sn and ^{112}Sn + ^{112}Sn reactions at 50 MeV/A [83]. At the same incident energy, isospin diffusion was investigated. We recall that isospin diffusion in HICs depends on the different N/Z asymmetries of the involved projectiles and targets, hence it is used to probe the symmetry energy [84–86]. The filled black circle shows the result from isospin diffusion observables measured for collisions at the lower beam energy of 35 MeV per nucleon [87]. Transverse collective flows of hydrogen and helium isotopes as well as intermediate-mass fragments, with $Z < 9$, have also been measured at an incident energy of 35 MeV/A in ^{70}Zn + ^{70}Zn, ^{64}Zn + ^{64}Zn, and ^{64}Ni + ^{64}Ni reactions and compared to transport calculations. The analysis yielded values denoted by the filled black squares [88].

The box labeled FRDM (finite-range droplet model) represents a refinement of the droplet model [89] and includes microscopic "shell" effects and the extra binding associated with $N = Z$ nuclei. The FRDM reproduces nuclear binding energies of known nuclei within 0.1% and allows the determination of both $S_0 = 32.5 \pm 0.5$ MeV and $L = 70 \pm 15$ MeV.

The other boxes in Fig. 9 represent experimental data obtained from measurements of the neutron skin thickness. In light nuclei, with $N \approx Z$, the neutrons and protons have similar density distributions. With increasing neutron number N, the radius of the neutron density distribution becomes larger than that of the protons, reflecting the pressure of the symmetry energy. The measurement of the neutron skin thickness is made on the stable nucleus ^{208}Pb, which has a closed neutron shell with $N = 126$ and a closed proton shell with $Z = 82$, hence it is very asymmetric and the neutron skin is very thick. The possibility of measurements of the neutron radius in ^{208}Pb by the experiment PREX at Jefferson Laboratory has been widely discussed [90]. The experiment should extract the value of the neutron radius in ^{208}Pb from parity-violating electron scattering. However, the experimental signature is very small, and the extracted thickness has a large statistical uncertainty. In the next few years, a second experimental run for PREX could reduce this large uncertainty [91].

Recent experimental data obtained by Zenihiro *et al.* [92] on the neutron skin thickness of ^{208}Pb deduced a value of $\delta R_{np} = 0.211^{+0.054}_{-0.063}$ fm. From the experiments constraints on

the symmetry energy were derived, and these are plotted in Fig. 9 as the short-dashed rectangular (blue) box labeled Pb($\vec{p},\vec{p}'$).

Finally, we mention the experimental data on the pygmy dipole resonance (PDR) in very neutron-rich nuclei such as ^{68}Ni and ^{132}Sn, which peaks at excitation energies well below the giant dipole resonance and exhausts about 5% of the energy-weighted sum rule [93]. In many models it has been found that this percentage is linearly dependent on the slope L of the symmetry energy. Values of $L = 64.8 \pm 15.7$ MeV and $S_0 = 32.2 \pm 1.3$ MeV were extracted in Ref. [94], using various models which connect L with the neutron skin thickness. Those constraints are shown in Fig. 9 as the long-dashed rectangle labeled PDR.

It is not clear to what extent all these constraints are compatible with each other, but it looks that most of the EOSs provide values consistent with the general trend, including the fss2 EOS.

IV. NEUTRON STAR STRUCTURE

In order to study the structure of NSs, we have to calculate the composition and the EOS of cold, neutrino-free, catalyzed matter. We require that the NS contains charge-neutral matter consisting of neutrons, protons, and leptons (e^-, μ^-) in β equilibrium and compute the EOS in the following standard way [95,96]: The Brueckner calculation yields the energy density of baryon/lepton matter as a function of the different partial densities,

$$\varepsilon(\rho_n,\rho_p,\rho_e,\rho_\mu) = (\rho_n m_n + \rho_p m_p) + (\rho_n + \rho_p)\frac{E}{A}(\rho_n,\rho_p) + \rho_\mu m_\mu + \frac{1}{2m_\mu}\frac{(3\pi^2\rho_\mu)^{5/3}}{5\pi^2} + \frac{(3\pi^2\rho_e)^{4/3}}{4\pi^2}, \quad (15)$$

where we have used ultrarelativistic and nonrelativistic approximations for the energy densities of electrons and muons, respectively. In this study, we adopted the parabolic approximation for E/A, Eq. (12). Knowing the energy density, Eq. (15), the various chemical potentials (of the species $i = n,p,e,\mu$) can be computed straightforwardly,

$$\mu_i = \frac{\partial\varepsilon}{\partial\rho_i}, \quad (16)$$

and the equations for β equilibrium,

$$\mu_i = b_i\mu_n - q_i\mu_e \quad (17)$$

(b_i and q_i denoting the baryon number and charge of species i), and charge neutrality,

$$\sum_i \rho_i q_i = 0, \quad (18)$$

allow one to determine the equilibrium composition $\{\rho_i\}$ at a given baryon density ρ and, finally, the EOS:

$$P(\rho) = \rho^2\frac{d}{d\rho}\frac{\varepsilon(\{\rho_i(\rho)\})}{\rho} = \rho\frac{d\varepsilon}{d\rho} - \varepsilon = \rho\mu_n - \varepsilon. \quad (19)$$

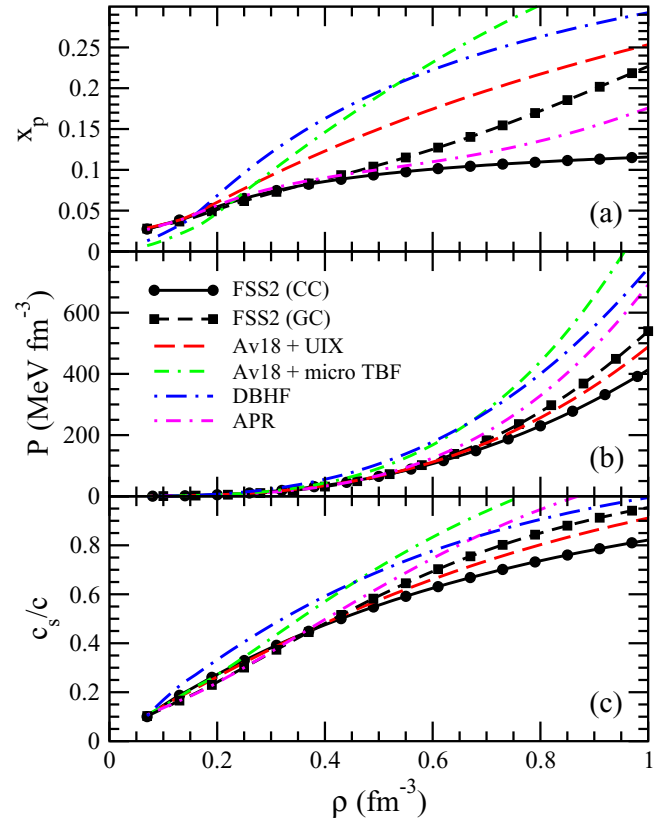

FIG. 10. (Color online) (a) Proton fraction x_p, (b) pressure P, and (c) speed of sound (in units of c) of β-stable nuclear matter for several EOSs as a function of the baryon density ρ.

In Fig. 10 we present the proton fraction x_p, the pressure P, and the sound velocity,

$$c_s = \sqrt{\frac{\partial P}{\partial\varepsilon}}, \quad (20)$$

as a function of the total baryon density in NS matter. The sound velocity can be used as a further test of a given EOS, since it should not exceed the speed of light c. One can see that the fss2 EOS becomes superluminal only at a very high density, which, as we will see, is actually not reached in the corresponding NS structure.

Once the EOS of the nuclear matter which is present throughout the NS is known, one can use the Tolman-Oppenheimer-Volkoff [96–98] equations for spherically symmetric NSs:

$$\frac{dp}{dr} = -\frac{Gm\varepsilon}{r^2}\frac{(1+p/\varepsilon)(1+4\pi r^3 p/m)}{1-2Gm/r}, \quad (21)$$

$$\frac{dm}{dr} = 4\pi r^2\varepsilon, \quad (22)$$

where G is the gravitational constant and $m(r)$ is the enclosed mass within a radius r. Given a starting density ε_c, one integrates these equations until the surface $r = R$, and the gravitational mass is obtained by $M_G = m(R)$. The EOS needed to solve the Tolman-Oppenheimer-Volkof equations is taken from the nuclear matter calculations as discussed above

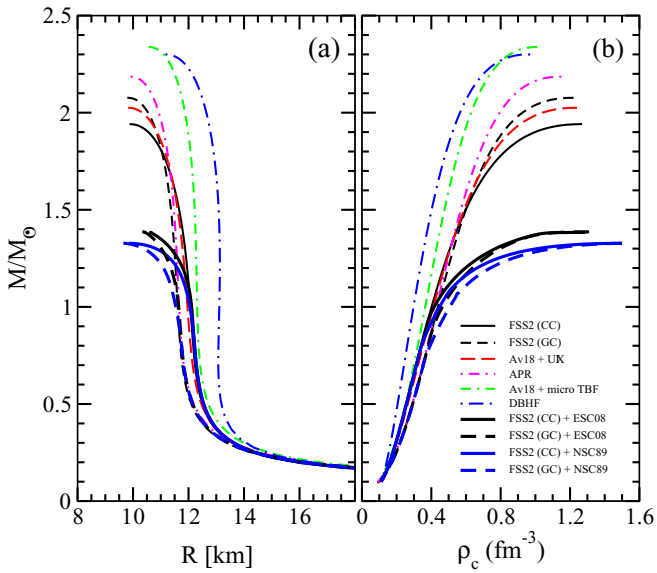

FIG. 11. (Color online) Neutron star mass as a function (a) of the radius or (b) of the central baryon density for several EOSs. Thin lines indicate results obtained with purely nucleonic EOSs, whereas thick lines show results for several EOSs including hyperons. See text for details.

for the liquid-core region and matched with the crust EOS, which has been taken from Refs. [99–101]. This matching occurs at about two-thirds the saturation density, where the EOS analytical fits of Eq. (13) are still accurate.

As is well known, the mass of the NS has a maximum value as a function of the radius (or central density), above which the star is unstable against collapse to a black hole. The value of the maximum mass depends on the nuclear EOS, so that the observation of a mass higher than the maximum mass allowed by a given EOS simply rules out that EOS. The fss2 EOS gives slightly different maximum masses for the gap choice and continuous cases, in line with their different stiffnesses at a high density. This gives a range of uncertainty for the maximum mass, which encompasses the largest mass observed up to now, $(2.01 \pm 0.04)M_\odot$ [102]. This is illustrated in Fig. 11, where the relation between mass and radius [Fig. 11(a)] or mass and central density [Fig. 11(b)] is displayed in comparison with the other considered EOSs (thin lines). The observed trend of the central density for all the EOSs is consistent with the corresponding $P(\rho)$ relation displayed in Fig. 10(b). As expected, with increasing incompressibility, the NS central density decreases for a given mass.

Finally, we illustrate the so-called "hyperon puzzle" with the fss2 model. Figure 11 (thick lines) shows the effect of allowing the appearance of hyperons in β-stable matter within our BHF approach [103,104]. Two nucleon-hyperon interactions, the Nijmegen NSC89 model [105] and the recent ESC08 model [106], are considered and combined with the fss2 NN potential in the approximate way explained in more detail in Ref. [103]; namely, the purely nucleonic BHF energy density obtained with fss2 is combined with the hyperonic contribution to the energy density evaluated with either the NSC89 or the ESC08 interaction, but together with the Argonne V_{18} potential plus nucleonic TBF. In this way the intermediate states in the nucleon-hyperon Bethe-Goldstone equation are treated approximately, but the overall error of the global results is expected to be small [103].

Figure 11 demonstrates that under these assumptions the NS maximum mass is practically insensitive to the choice of the NN interaction, but determined by the nucleon-hyperon interaction. This is due to a well-known compensation mechanism that is clearly shown in Fig. 11(a): The slightly stiffer fss2 gap-choice model [thick dashed (black and blue) curves] causes an earlier onset of hyperons and a stronger softening than the fss2 continuous-choice model (solid curves). In any situation the maximum mass is much smaller than the current observational values.

V. SUMMARY AND DISCUSSION

We have derived the nuclear matter EOS within the BBG approach up to the THL level of approximation, starting from an NN interaction based on quark-quark and quark-meson interactions. An intrinsic uncertainty in the approach is related to the choice of the auxiliary s.p. potential. Within this uncertainty the saturation point is well reproduced without any additional parameters with respect to the interaction, which is able also to reproduce the binding of three- and four-nucleon systems. At higher energies the interaction should be improved in some channels, in particular, $^3P_2$-$^3F_2$, which is relevant for the high-density part of the EOS and, therefore, for NS.

The symmetry energy as a function of the density up to saturation, its value and slope at saturation, and the incompressibility of symmetric matter at saturation compare favorably well with the phenomenological constraints. Above saturation the EOS is compatible with the flow data in HICs at intermediate energies, up to about four times the saturation density.

As discussed, a warning about these calculations is the observation that two-hole-line and THL diagram contributions become comparable at higher densities, which casts some doubt on the convergence of the BBG expansion. However, this is mainly due to the behavior of the two-hole-line contribution, which saturates or even decreases at higher densities, due to the compensation between positive and negative contributions. This indicates that the degree of convergence cannot be estimated in a straightforward way. Within the present many-body treatment this is probably the main source of uncertainty in the results.

However, let us note that up to a few times the saturation density the EOS calculated with the continuous and gap choices agree very well. In particular, for symmetric matter the agreement extends up to the maximal density used in NS calculations. This fact can be considered a good indication of the convergence of the expansion, because this agreement would be exactly true if convergence is indeed reached. For similar reasons the mass-radius relationships in NSs are quite close for the two choices, which supports the validity of these results.

The EOS can be considered relatively soft, but despite that, the NS maximum mass is compatible with the current observed NS maximum mass of about two solar masses [102]. Phenomenology seems then to validate this microscopically derived EOS, at least up to a few times the saturation density.

However, there are some theoretical caveats to be considered. It can be expected that quark matter appears in the center of massive NSs. To describe these "hybrid" NSs one needs to know the quark matter EOS. It turns out that many models for deconfined quark matter produce an EOS that is too soft to support a NS of mass compatible with observations [107–113]. The quark-quark interaction in the deconfined phase must then be repulsive enough to stiffen the EOS, and indeed, with a suitable quark-quark interaction, mixed quark-nucleon matter can have an EOS compatible with two solar masses or more [114,115].

An additional problem arises if strange matter is introduced in the NS matter. It turns out that BHF calculations using realistic hyperon-nucleon interactions known in the literature produce a NS matter EOS that is too soft, and the maximum mass is reduced to well below the observational limit [103,104]. Although hyperon-hyperon interactions and, in particular, hyperonic TBFs are poorly known, these results pose a "hyperon puzzle." An EOS based on relativistic mean-field models can solve the problem [116–118] with a proper choice of parameters. Also, modifications of the hyperon-nucleon interaction, including TBFs, could provide a remedy for the too soft EOS [119,120]. All these methods introduce quark-quark or nucleon-hyperon and hyperon-hyperon interactions that stiffen the EOS enough at high densities.

In this respect, it would be of particular relevance to perform BBG calculations up to the THL level with the quark-model baryon-baryon interaction fss2 extended to the strange sector [44]. This difficult problem must be left for a future long-term project.

ACKNOWLEDGMENTS

K.F. would like to express his gratitude to Prof. T. Rijken for providing him with the Nijmegen phase shift analysis data and the program for the χ^2 analysis. Partial support comes from "NewCompStar", European Cooperation in Science and Technology (COST) Action MP1304.

APPENDIX: DEUTERON WAVE FUNCTION

In this appendix, we basically follow the notation in Ref. [38]. First, we solve the Lippmann-Schwinger RGM equation for the deuteron:

$$(\gamma^2+k^2)f_\ell(k) = -M_N \frac{4\pi}{(2\pi)^3} \sum_{\ell'} \int_0^\infty dq\, q^2\, V_{\ell\ell'}(k,q) f_{\ell'}(q). \tag{A1}$$

Here we use the nonrelativistic expression $\varepsilon_d = \gamma^2/M_N$ as the deuteron binding energy. The relativistic correction is of order ε_d^2/M_N, which corresponds to a difference of a few keV [53]. The total wave function is

$$\Psi_d^{1M}(\boldsymbol{k}) = \left[f_0(k)\mathscr{Y}_{01}^{1M}(\hat{\boldsymbol{k}}) + f_2(k)\mathscr{Y}_{21}^{1M}(\hat{\boldsymbol{k}})\right]\zeta_0^0, \tag{A2}$$

where $\mathscr{Y}_{LS}^{JM}(\hat{\boldsymbol{k}})$ are spin-spherical harmonics and the isospin function is denoted $\zeta_T^{M_T}$. In coordinate space, we have

$$\Psi_d^{1M}(\boldsymbol{r}) = \left[(u_0(r)/r)\mathscr{Y}_{01}^{1M}(\hat{\boldsymbol{r}}) + (u_2(r)/r)\mathscr{Y}_{21}^{1M}(\hat{\boldsymbol{r}})\right]\zeta_0^0. \tag{A3}$$

They are related by the Fourier transform

$$u_\ell(r) = \sqrt{2/\pi}\; i^\ell \int_0^\infty dk\, k^2 r j_\ell(kr) f_\ell(k). \tag{A4}$$

The normalization is

$$\sum_{\ell=0,2} \int_0^\infty dr\; u_\ell^2(r) = \sum_{\ell=0,2} \int_0^\infty dk\, k^2\, f_\ell^2(k) = 1. \tag{A5}$$

The deuteron wave functions are parametrized in the following way, as in Refs. [38] and [53]:

$$f_{\ell\alpha}(k) = \sum_{j=1}^{n} \begin{Bmatrix} C_j \\ D_j \end{Bmatrix} \sqrt{\frac{2}{\pi}} \frac{1}{k^2+\gamma_j^2} \quad \text{for} \quad \begin{cases} \ell = 0, \\ \ell = 2; \end{cases} \tag{A6}$$

$$u_{\ell\alpha}(r) = \sum_{j=1}^{n} \begin{Bmatrix} C_j e^{-\gamma_j r} \\ D_j e^{-\gamma_j r}\left(1+\frac{3}{\gamma_j r}+\frac{3}{(\gamma_j r)^2}\right) \end{Bmatrix} \quad \text{for} \quad \begin{cases} \ell = 0, \\ \ell = 2. \end{cases} \tag{A7}$$

The range parameters are chosen as $\gamma_j = \gamma + (j-1)\gamma_0$, with $\gamma_0 = 0.9$ fm^{-1} and $n = 11$.

For $r \to \infty$, the deuteron wave functions have the form $u_0(r) \to A_S e^{-\gamma_1 r}$ and $u_2(r) \to A_D e^{-\gamma_1 r}[1 + 3/(\gamma_1 r) + 3/(\gamma_1 r)^2]$, where $A_S = C_1$ and $A_D = D_1$. The asymptotic D/S ratio is given by $\eta = A_S/A_D$. The boundary conditions $u_0(r) \to r$ and $u_2(r) \to r^3$ as $r \to 0$ lead to one constraint for the C_j and three constraints for the D_j [121]. These constraints for the last C_j and the last three D_j are explicitly written in Eqs. (C.7) and (C.8) in Ref. [53]. The values of γ_j, C_j, and D_j are listed in Table VIII. The accuracy of the parametrization is characterized by

$$\left\{\int_0^\infty dk\, k^2 [f_0(k) - f_{0\alpha}(k)]^2\right\}^{1/2} = 1.9 \times 10^{-4}, \tag{A8}$$

$$\left\{\int_0^\infty dk\, k^2 [f_2(k) - f_{2\alpha}(k)]^2\right\}^{1/2} = 2.3 \times 10^{-4}. \tag{A9}$$

The quadrupole moment Q_d, the root-mean-square radius R_d, and the D-state probability P_D are calculated using Eqs. (C.16), (C.17), and (C.18) in Ref. [53], respectively.

TABLE VIII. Range parameters γ_j and coefficients C_j and D_j for the parametrized deuteron wave function. Values in parentheses are calculated from the boundary conditions.

j	γ_j	C_j	D_j
1	0.2314	0.8803	0.2218×10^{-1}
2	1.1314	–0.2235	–0.4637
3	2.0314	–0.2501	0.1776
4	2.9314	-0.1658×10^2	-0.1294×10^2
5	3.8314	0.1694×10^3	0.1192×10^3
6	4.7314	-0.9160×10^3	-0.5884×10^3
7	5.6314	0.2592×10^4	0.1611×10^4
8	6.5314	-0.4095×10^4	-0.2503×10^4
9	7.4314	0.3678×10^4	(0.2214×10^4)
10	8.3314	-0.1766×10^4	(-0.1043×10^4)
11	9.2314	(0.3530×10^3)	(0.2040×10^3)

[1] For a brief review see M. Baldo and G. F. Burgio, Rep. Prog. Phys. **75**, 026301 (2012).
[2] A. Akmal, V. R. Pandharipande, and D. G. Ravenhall, Phys. Rev. C **58**, 1804 (1998).
[3] T. Gross-Boelting, C. Fuchs, and A. Faessler, Nucl. Phys. A **648**, 105 (1999).
[4] B. D. Day, Phys. Rev. C **24**, 1203 (1981); Phys. Rev. Lett. **47**, 226 (1981).
[5] H. Q. Song, M. Baldo, G. Giansiracusa, and U. Lombardo, Phys. Rev. Lett. **81**, 1584 (1998).
[6] M. Baldo, G. Giansiracusa, U. Lombardo, and H. Q. Song, Phys. Lett. B **473**, 1 (2000); M. Baldo, A. Fiasconaro, H. Q. Song, G. Giansiracusa, and U. Lombardo, Phys. Rev. C **65**, 017303 (2001).
[7] R. Sartor, Phys. Rev. C **73**, 034307 (2006).
[8] J. Carlson, V. R. Pandharipande, and R. B. Wiringa, Nucl. Phys. A **401**, 59 (1983); R. Schiavilla, V. R. Pandharipande, and R. B. Wiringa, *ibid.* **449**, 219 (1986).
[9] G. Taranto, M. Baldo, and G. F. Burgio, Phys. Rev. C **87**, 045803 (2013).
[10] P. Grangé, A. Lejeune, M. Martzolff, and J.-F. Mathiot, Phys. Rev. C **40**, 1040 (1989); W. Zuo, A. Lejeune, U. Lombardo, and J.-F. Mathiot, Nucl. Phys. A **706**, 418 (2002); Eur. Phys. J. A **14**, 469 (2002).
[11] Z. H. Li, U. Lombardo, H.-J. Schulze, W. Zuo, L. W. Chen, and H. R. Ma, Phys. Rev. C **74**, 047304 (2006).
[12] S. Weinberg, Phys. Lett. B **251**, 288 (1990); Nucl. Phys. B **363**, 3 (1991); Phys. Lett. B **295**, 114 (1992); Phys. Rev. **166**, 1568 (1968).
[13] D. R. Entem and R. Machleidt, Phys. Rev. C **68**, 041001 (2003).
[14] M. P. Valderrama and D. R. Phillips, Phys. Rev. Lett. **114**, 082502 (2015).
[15] H. Leutwyler, Ann. Phys. **235**, 165 (1994).
[16] Ulf-G. Meissner, Nucl. Phys. A **751**, 149 (2005).
[17] E. Epelbaum, H. W. Hammer, and Ulf-G. Meissner, Rev. Mod. Phys. **81**, 1773 (2009).
[18] T. Otsuka, T. Suzuki, J. D. Holt, A. Schwenk, and Y. Akaishi, Phys. Rev. Lett. **105**, 032501 (2010); J. D. Holt, J. Menéndez, and A. Schwenk, *ibid.* **110**, 022502 (2013).
[19] K. Hebeler, S. K. Bogner, R. J. Furnstahl, A. Nogga, and A. Schwenk, Phys. Rev. C **83**, 031301 (2011).
[20] C. Drischler, V. Somà, and A. Schwenk, Phys. Rev. C **89**, 025806 (2014).
[21] K. Hebeler and A. Schwenk, Phys. Rev. C **82**, 014314 (2010).
[22] A. Carbone, A. Polls, and A. Rios, Phys. Rev. C **88**, 044302 (2013).
[23] A. Ekström, G. Baardsen, C. Forssen, G. Hagen, M. Hjorth-Jensen, G. R. Jansen, R. Machleidt, W. Nazarewicz, T. Papenbrock, J. Sarich, and S. M. Wild, Phys. Rev. Lett. **110**, 192502 (2013).
[24] L. Coraggio, J. W. Holt, N. Itaco, R. Machleidt, L. E. Marcucci, and F. Sammarruca, Phys. Rev. C **89**, 044321 (2014).
[25] T. A. Lähde, E. Epelbaum, H. Krebs, D. Lee, Ulf-G. Meissner, and G. Rupak, Phys. Lett. B **732**, 110 (2014).
[26] A. Ekström, G. R. Jansen, K. A. Wendt, G. Hagen, T. Papenbrock, B. D. Carlsson, C. Forssen, M. Hjorth-Jensen, P. Navratil, and W. Nazarewicz, Phys. Rev. C **91**, 051301(R) (2015).
[27] J. E. Lynn, I. Tews, J. Carlson, S. Gandolfi, A. Gezerlis, K. E. Schmidt, and A. Schwenk, arXiv:1509.03470 [nucl-th].
[28] G. Hagen, T. Papenbrock, A. Ekström, K. A. Wendt, G. Baardsen, S. Gandolfi, M. Hjorth-Jensen, and C. J. Horowitz, Phys. Rev. C **89**, 014319 (2014).
[29] G. Baardsen, A. Ekström, G. Hagen, and M. Hjorth-Jensen, Phys. Rev. C **88**, 054312 (2013).
[30] S. Binder, P. Piecuch, A. Calci, J. Langhammer, P. Navratil, and R. Roth, Phys. Rev. C **88**, 054319 (2013).
[31] M. Oka and K. Yazaki, Phys. Lett. B **90**, 41 (1980); Prog. Theor. Phys. **66**, 556 (1981); **66**, 572 (1981); in *Quarks and Nuclei*, edited by W. Weise Singapore, 1984), p. 489.
[32] C. W. Wong, Phys. Rep. **136**, 1 (1986).
[33] M. Oka, K. Shimizu, and K. Yazaki, Nucl. Phys. A **464**, 700 (1987).
[34] K. Shimizu, Rep. Prog. Phys. **52**, 1 (1989).
[35] K. Shimizu, S. Takeuchi, and A. J. Buchmann, Prog. Theor. Phys. Suppl. **137**, 43 (2000).
[36] A. Valcarce, H. Garcilazo, F. Fernández, and P. González, Rep. Prog. Phys. **68**, 965 (2005).
[37] Y. Fujiwara, Y. Suzuki, and C. Nakamoto, Prog. Part. Nucl. Phys. **58**, 439 (2007).
[38] Y. Fujiwara, T. Fujita, M. Kohno, C. Nakamoto, and Y. Suzuki, Phys. Rev. C **65**, 014002 (2001).
[39] Y. Fujiwara, Y. Suzuki, M. Kohno, and K. Miyagawa, Phys. Rev. C **77**, 027001 (2008).
[40] Y. Fujiwara and K. Fukukawa, Few-Body Syst. **54**, 2357 (2013).
[41] Y. Fujiwara, Few-Body Syst. **55**, 993 (2014).
[42] M. Baldo and K. Fukukawa, Phys. Rev. Lett. **113**, 242501 (2014).
[43] Y. Fujiwara and K. Fukukawa, Prog. Theor. Phys. **124**, 433 (2010).
[44] Y. Fujiwara, M. Kohno, C. Nakamoto, and Y. Suzuki, Phys. Rev. C **64**, 054001 (2001).
[45] M. Baldo, *Nuclear Methods and the Nuclear Equation of State*. International Review of Nuclear Physics, Vol. 8 (World Scientific, Singapore, 1999).
[46] Y. Fujiwara, C. Nakamoto, and Y. Suzuki, Phys. Rev. Lett. **76**, 2242 (1996); Phys. Rev. C **54**, 2180 (1996).
[47] T. Fujita, Y. Fujiwara, C. Nakamoto, and Y. Suzuki, Prog. Theor. Phys. **100**, 931 (1998).
[48] R. A. Bryan and B. L. Scott, Phys. Rev. **164**, 1215 (1967).
[49] Y. Fujiwara, M. Kohno, T. Fujita, C. Nakamoto, and Y. Suzuki, Prog. Theor. Phys. **103**, 755 (2000).
[50] Y. Suzuki, H. Matsumura, M. Orabi, Y. Fujiwara, P. Descouvemont, M. Theeten, and D. Baye, Phys. Lett. B **659**, 160 (2008).
[51] K. Fukukawa, Y. Fujiwara, and Y. Suzuki, Mod. Phys. Lett. A **24**, 1035 (2009).
[52] R. B. Wiringa, V. G. J. Stoks, and R. Schiavilla, Phys. Rev. C **51**, 38 (1995).
[53] R. Machleidt, Phys. Rev. C **63**, 024001 (2001).
[54] NN-OnLine; http://nn-online.org.
[55] V. G. J. Stoks, R. A. M. Klomp, M. C. M. Rentmeester, and J. J. de Swart, Phys. Rev. C **48**, 792 (1993).
[56] R. A. Arndt, L. D. Roper, R. A. Bryan, R. B. Clark, B. J. VerWest, and P. Signell, Phys. Rev. D **28**, 97 (1983).
[57] R. A. Arndt, J. S. Hyslop III, and L. D. Roper, Phys. Rev. D **35**, 128 (1987).
[58] R. A. Arndt, L. D. Roper, R. L. Workman, and M. W. McNaughton, Phys. Rev. D **45**, 3995 (1992).
[59] R. A. Arndt, I. I. Strakovsky, and R. L. Workman, SAID, Scattering Analysis Interactive Dial-in computer facility,

Virginia Polytechnic Institute and George Washington University, solution SM99 (1999).
[60] C. M. Vincent and S. C. Phatak, Phys. Rev. C **10**, 391 (1974).
[61] Y. Fujiwara and K. Fukukawa, Prog. Theor. Phys. **128**, 301 (2012).
[62] T. Rijken (private communication).
[63] L. J. Allen, H. Fieldeldey, and N. J. McGurk, J. Phys. G **4**, 353 (1978).
[64] M. Kohno, J. Phys. G **9**, L85 (1983).
[65] R. Machleidt, Adv. Nucl. Phys. **19**, 189 (1989).
[66] O. Dumbrajs, R. Koch, H. Pilkuhn, G. C. Oades, H. Behrens, J. J. de Swart, and P. Kroll, Nucl. Phys. B **216**, 277 (1983).
[67] F. Schmidt-Kaler, D. Leibfried, M. Weitz, and T. W. Hänsch, Phys. Rev. Lett. **70**, 2261 (1993).
[68] K. Pachucki, M. Weitz, and T. W. Hänsch, Phys. Rev. A **49**, 2255 (1994).
[69] J. Martorell, D. W. L. Sprung, and D. C. Zheng, Phys. Rev. C **51**, 1127 (1995).
[70] T. E. O. Ericson and M. Rosa-Clot, Nucl. Phys. A **405**, 497 (1983).
[71] D. M. Bishop and L. M. Cheung, Phys. Rev. A **20**, 381 (1979).
[72] N. L. Rodning and L. D. Knutson, Phys. Rev. C **41**, 898 (1990).
[73] T. Cheon and E. F. Redish, Phys. Rev. C **39**, 331 (1989); R. Sartor, *ibid.* **54**, 809 (1996); K. Suzuki, R. Okamoto, M. Kohno, and S. Nagata, Nucl. Phys. A **665**, 92 (2000).
[74] M. Baldo, I. Bombaci, L. S. Ferreira, G. Giansiracusa, and U. Lombardo, Phys. Rev. C **43**, 2605 (1991).
[75] I. Bombaci and U. Lombardo, Phys. Rev. C **44**, 1892 (1991).
[76] R. Rajaraman and H. Bethe, Rev. Mod. Phys. **39**, 745 (1967).
[77] B. D. Day, Phys. Rev. **187**, 1269 (1969).
[78] R. V. Reid, Ann. Phys. **50**, 411 (1968).
[79] P. Danielewicz, R. Lacey, and W. Lynch, Science **298**, 1592 (2002).
[80] C. Fuchs, Prog. Part. Nucl. Phys. **56**, 1 (2006).
[81] P. Danielewicz and J. Lee, Nucl. Phys. A **922**, 1 (2014).
[82] M. B. Tsang, J. R. Stone, F. Camera, P. Danielewicz, S. Gandolfi, K. Hebeler, C. J. Horowitz, J. Lee, W. G. Lynch, Z. Kohley, R. Lemmon, P. Moller, T. Murakami, S. Riordan, X. Roca-Maza, F. Sammarruca, A. W. Steiner, I. Vidana, and S. J. Yennello, Phys. Rev. C **86**, 015803 (2012).
[83] M. A. Famiano, T. Liu, W. G. Lynch, M. Mocko, A. M. Rogers, M. B. Tsang, M. S. Wallace, R. J. Charity, S. Komarov, D. G. Sarantites, L. G. Sobotka, and G. Verde, Phys. Rev. Lett. **97**, 052701 (2006).
[84] M. B. Tsang, C. K. Gelbke, X. D. Liu, W. G. Lynch, W. P. Tan, G. Verde, H. S. Xu, W. A. Friedman, R. Donangelo, S. R. Souza, C. B. Das, S. Das Gupta, and D. Zhabinsky, Phys. Rev. C **64**, 054615 (2001).
[85] T. X. Liu, W. G. Lynch, M. B. Tsang, X. D. Liu, R. Shomin, W. P. Tan, G. Verde, A. Wagner, H. F. Xi, H. S. Xu, B. Davin, Y. Larochelle, R. T. de Souza, R. J. Charity, and L. G. Sobotka, Phys. Rev. C **76**, 034603 (2007).
[86] B.-A. Li, L.-W. Chen, and C. M. Ko, Phys. Rep. **464**, 113 (2008).
[87] Z. Y. Sun, M. B. Tsang, W. G. Lynch, G. Verde, F. Amorini, L. Andronenko, M. Andronenko, G. Cardella, M. Chatterje, P. Danielewicz, E. De Filippo, P. Dinh, E. Galichet, E. Geraci, H. Hua, E. La Guidara, G. Lanzalone, H. Liu, F. Lu, S. Lukyanov, C. Maiolino, A. Pagano, S. Piantelli, M. Papa, S. Pirrone, G. Politi, F. Porto, F. Rizzo, P. Russotto, D. Santonocito, and Y. X. Zhang, Phys. Rev. C **82**, 051603(R) (2010).
[88] Z. Kohley, L. W. May, S. Wuenschel, M. Colonna, M. Di Toro, M. Zielinska-Pfabe, K. Hagel, R. Tripathi, A. Bonasera, G. A. Souliotis, D. V. Shetty, S. Galanopoulos, M. Mehlman, W. B. Smith, S. N. Soisson, B. C. Stein, and S. J. Yennello, Phys. Rev. C **83**, 044601 (2011).
[89] P. Möller, W. D. Myers, H. Sagawa, and S. Yoshida, Phys. Rev. Lett. **108**, 052501 (2012).
[90] C. J. Horowitz, Phys. Rev. C **57**, 3430 (1998); Eur. Phys. J. A **30**, 303 (2006); C. J. Horowitz, S. J. Pollock, P. A. Souder, and R. Michaels, Phys. Rev. C **63**, 025501 (2001).
[91] P. A. Souder *et al.*, PREX II experimental proposal to Jefferson Laboratory, PAC38; http://hallaweb.jlab.org/parity/prex/prexII.pdf.
[92] J. Zenihiro, H. Sakaguchi, T. Murakami, M. Yosoi, Y. Yasuda, S. Terashima, Y. Iwao, H. Takeda, M. Itoh, H. P. Yoshida, and M. Uchida, Phys. Rev. C **82**, 044611 (2010); J. Zenihiro, Ph.D. thesis, Kyoto University (2011).
[93] A. Klimkiewicz, N. Paar, P. Adrich, M. Fallot, K. Boretzky, T. Aumann, D. Cortina-Gil, U. Datta Pramanik, Th. W. Elze, H. Emling, H. Geissel, M. Hellström, K. L. Jones, J. V. Kratz, R. Kulessa, C. Nociforo, R. Palit, H. Simon, G. Surówka, K. Sümmerer, D. Vretenar, and W. Waluś, Phys. Rev. C **76**, 051603(R) (2007).
[94] A. Carbone, G. Colò, A. Bracco, L.-G. Cao, P. F. Bortignon, F. Camera, and O. Wieland, Phys. Rev. C **81**, 041301(R) (2010).
[95] M. Baldo, I. Bombaci, and G. F. Burgio, Astron. Astrophys. **328**, 274 (1997).
[96] S. L. Shapiro and S. A. Teukolsky, *Black Holes, White Dwarfs, and Neutron Stars* (John Wiley & Sons, New York, 1983).
[97] R. C. Tolman, Phys. Rev. **55**, 364 (1939).
[98] J. R. Oppenheimer and G. M. Volkoff, Phys. Rev. **55**, 374 (1939).
[99] J. W. Negele and D. Vautherin, Nucl. Phys. A **207**, 298 (1973).
[100] R. P. Feynman, N. Metropolis, and E. Teller, Phys. Rev. **75**, 1561 (1949).
[101] G. Baym, C. Pethick, and D. Sutherland, Astrophys. J. **170**, 299 (1971).
[102] J. Antoniadis *et al.*, Science **340**, 1233232 (2013).
[103] H.-J. Schulze, A. Polls, A. Ramos, and I. Vidaña, Phys. Rev. C **73**, 058801 (2006).
[104] H.-J. Schulze and T. Rijken, Phys. Rev. C **84**, 035801 (2011).
[105] P. M. M. Maessen, T. A. Rijken, and J. J. de Swart, Phys. Rev. C **40**, 2226 (1989).
[106] T. Rijken, M. Nagels, and Y. Yamamoto, Prog. Theor. Phys. Suppl. **185**, 14 (2010); Few-Body Syst. **54**, 801 (2013).
[107] G. F. Burgio, M. Baldo, P. K. Sahu, A. B. Santra, and H.-J. Schulze, Phys. Lett. B **526**, 19 (2002).
[108] G. F. Burgio, M. Baldo, P. K. Sahu, and H.-J. Schulze, Phys. Rev. C **66**, 025802 (2002).
[109] M. Baldo, M. Buballa, G. F. Burgio, F. Neumann, M. Oertel, and H.-J. Schulze, Phys. Lett. B **562**, 153 (2003).
[110] C. Maieron, M. Baldo, G. F. Burgio, and H.-J. Schulze, Phys. Rev. D **70**, 043010 (2004).
[111] O. E. Nicotra, M. Baldo, G. F. Burgio, and H.-J. Schulze, Phys. Rev. D **74**, 123001 (2006).
[112] M. Baldo, G. F. Burgio, P. Castorina, S. Plumari, and D. Zappalá, Phys. Rev. D **78**, 063009 (2008).
[113] H. Chen, M. Baldo, G. F. Burgio, and H.-J. Schulze, Phys. Rev. D **84**, 105023 (2011).
[114] M. G. Alford, S. Han, and M. Prakash, Phys. Rev. D **88**, 083013 (2013).

[115] A. Li, W. Zuo, and G. X. Peng, Phys. Rev. C **91**, 035803 (2015).
[116] I. Bednarek, P. Haensel, J. L. Zdunik, M. Bejger, and R. Mańka, Astron. Astrophys. **543**, A157 (2012).
[117] K. A. Maslov, E. E. Kolomeitsev, and D. N. Voskresensky, Phys. Lett. B **748**, 369 (2015).
[118] M. Oertel, C. Providência, F. Gulminelli, and A. R. Raduta, J. Phys. G **42**, 075202 (2015).
[119] D. Lonardoni, A. Lovato, S. Gandolfi, and F. Pederiva, Phys. Rev. Lett. **114**, 092301 (2015).
[120] Y. Yamamoto, T. Furumoto, N. Yasutake, and T. A. Rijken, Phys. Rev. C **90**, 045805 (2014).
[121] M. Lacombe, B. Loiseau, J. Richard, R. Vinh Mau, J. Côté, P. Pirès, and R. de Tourreil, Phys. Lett. B **101**, 139 (1981).